ACS Catalysis

Research Article

pubs.acs.org/acscatalysis

Dynamic Methane Partial Oxidation Using a Fe_2O_3@$La_{0.8}Sr_{0.2}FeO_{3-\delta}$ Core−Shell Redox Catalyst in the Absence of Gaseous Oxygen

Luke M. Neal, Arya Shafiefarhood, and Fanxing Li*

Department of Chemical and Biomolecular Engineering, North Carolina State University, 911 Partners Way, Raleigh, North Carolina 27695-7905, United States

Supporting Information

ABSTRACT: Chemical looping reforming partially oxidizes methane into syngas through cyclic redox reactions of an active lattice-oxygen (O^{2-}) containing redox catalyst. The avoidance of direct contact between methane and steam and/or gaseous oxygen has the potential to eliminate the energy consumption for generating these oxidants, thereby increasing methane conversion efficiency. This article investigates redox catalysts comprised of iron oxide core covered with lanthanum strontium ferrite (LSF) shell. The iron oxide core serves as the primary source of lattice-oxygen, whereas the LSF shell provides an active surface and facilitates O^{2-} and electron conductions. These core−shell materials have the promise to provide higher selectivity for methane conversion with lower solid circulation rates than traditional redox catalysts. Methane oxidation by this catalyst exhibits four distinct regions, i.e. deep oxidation; competing deep and selective oxidation; selective oxidation with autoactivation; and methane decomposition. Further investigations indicate that the evolution of "loose" lattice oxygen from the bulk contributes to deep oxidation, whereas reduced surface iron species are responsible for selective methane oxidation.

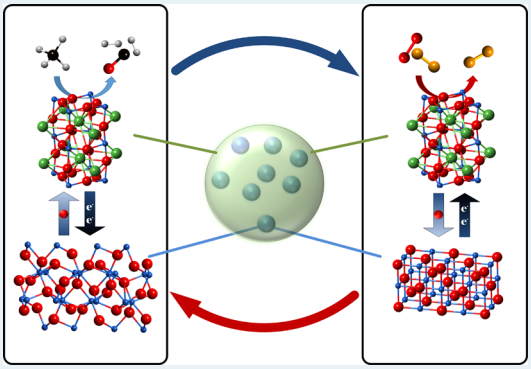

KEYWORDS: *methane reforming, chemical looping, redox catalyst, mixed ionic-electronic conductor, core−shell, perovskite*

INTRODUCTION

The relative abundance of natural gas compared to petroleum has led to renewed interest in converting methane to value-added products.[1−4] Much work has focused on one step conversion of methane, including methane to oxygenates,[5,6] oxidative coupling of methane,[7,8] and methane aromatization.[9−11] Compared to these one-step approaches, which are at the early stages of development, multistep or indirect methane conversion processes have been industrially implemented for the production of hydrogen, liquid fuels, and other chemicals.[12−14] As the first step of these indirect processes, methane reforming, which converts methane into syngas, represents a key unit operation that is both energy and capital intensive.[12,15] While the reforming step can be accomplished via multiple routes in the presence of gaseous oxidants such as steam and/or oxygen, the generation of these oxidants can incur a significant energy penalty.[12,15] As an alternative approach, autothermal chemical looping reforming (CLR) does not have these drawbacks since the oxygen used for methane partial oxidation is "captured" from air into the lattice of a redox catalyst, thereby avoiding the need for steam generation or cryogenic air separation.[16−20] Figure 1 illustrates a simplified schematic of the CLR process. Operated under a cyclic redox mode, the redox catalyst, a.k.a. oxygen carrier, partially oxidizes methane into syngas with its active lattice oxygen (O^{2-}). The lattice oxygen consumed for methane oxidation is subsequently replenished in a separate reactor.

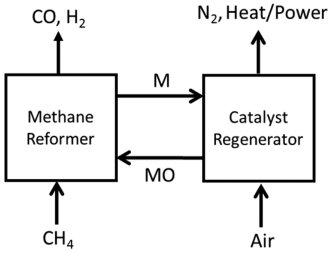

Figure 1. Simplified schematic of the CLR process.

Since the redox catalyst is the key to the CLR process, significant research efforts have focused on catalyst selection and development. To date, most redox catalysts/oxygen carriers are composed of a primary oxide to store active lattice oxygen and an "inert" ceramic support to enhance the activity and stability of the primary oxide. Among the various primary oxides, nickel oxide has attracted the most attention due to its high activity and selectively for methane partial oxidation.[18,21−23] The challenge of NiO based redox catalysts, however, resides in their high tendency for coke formation, high cost, and health concerns.[16,24] Compared to NiO, iron oxides are cheaper and environmentally benign. However, iron

Received: June 16, 2014
Revised: August 26, 2014
Published: August 27, 2014

   dx.doi.org/10.1021/cs5008415 | ACS Catal. 2014, 4, 3560−3569

oxides, in both pure and inert-supported forms, are significantly less active for methane oxidation.[16,17] They also exhibit low selectivity toward syngas.[25] Our recent studies have indicated that these limitations can be addressed through the use of tailored "support" material. For instance, perovskite-structured mixed ionic-electronic conductive (MIEC) supports, such as lanthanum strontium ferrite (LSF),[26,27] are found to significantly enhance the activity and selectivity of iron based redox catalysts.[28]

Besides being effective as a supports, perovskite materials such as LSF and LF (lanthanum ferrite) have been investigated as standalone redox catalysts for CLR of methane due to their ability to release lattice oxygen under varying external oxygen partial pressure (P_{O2}).[29−33] Dai et al. reported that lanthanum ferrite ($LaFeO_3$) was active and selective for syngas formation from methane.[34] They attributed the nonselective deep oxidation to surface oxygen. It was also noted that after an initial period of deep oxidation, the activity of the catalyst increased until oxygen depletion and coke formation.[34] Mihai et al. reported a similar redox performance of LF based redox catalyst. A larger crystallite size was reported to improve activity and oxygen carrying capacity (percentage of removable O^{2-}) of the catalyst.[34,35] The authors also concluded that bulk O^{2-} conduction was fast enough to maintain equilibrium between the bulk and the surface. Moreover, oxygen coverage on the surface determined the selectivity toward desired (syngas) and undesired (CO_2, H_2O, coke) products. He et al. reported that mixed-conducting $La_{1-x}Sr_xFeO_{3-\delta}$ systems were selective and highly regenerable.[36]

Although the above-mentioned perovskites are active and selective for CLR, they have limited oxygen carrying capacity (~10 wt %) when compared to Fe_2O_3 (30 wt %) or Co_3O_4 (27 wt %).[17,37,38] In addition, mixed-conductive perovskites often contain rare earth metals, which can be costly. Therefore, redox catalysts that take advantage of the high activity/selectivity of perovskites and low cost/high oxygen capacity of iron oxides are highly desirable for CLR processes. Our previous work has shown that $La_{0.8}Sr_{0.2}FeO_3$ (LSF), a mixed ionic electrical conductor (MIEC) support,[27] enhances the activity of iron oxide for methane conversion by nearly 2 orders of magnitude.[28,39] The high activity is attributed to enhanced O^{2-} and electron transports facilitated by the LSF support.[40] Preliminary data also indicated that redox catalysts with the Fe_2O_3@LSF structure have excellent activity, selectivity, and coke resistance.[25]

In the current work, core−shell Fe_2O_3@LSF, composite Fe_2O_3:LSF, and single-phase LSF based redox catalysts are characterized in detail in order to obtain mechanistic insights for the improved redox performance. The core−shell redox catalyst is found to be highly effective for syngas production. X-ray photoelectron spectroscopy (XPS) measurements indicate stable surface coverage of perovskites for the core−shell redox catalyst over 50 redox cycles. Further investigation of methane-redox catalyst reactions reveals a highly dynamic reaction scheme that can be divided into four regions, i.e. (i) a deep methane oxidation region attributable to loosely bonded lattice oxygen in addition to surface oxygen species; (ii) a competing deep and selective oxidation region attributable to relatively high surface oxygen coverage and abundant bulk lattice oxygen supply; (iii) a selective oxidation region with autoactivation attributable to reduced surface iron species and tightly bonded lattice oxygen species; and (iv) a methane decomposition and coke formation region resulting from O^{2-} depletion.

EXPERIMENTAL SECTION

Catalyst Preparation. Catalysts are prepared by a modified Pechini method described in previous work.[25] Briefly, stoichiometric amounts of nitrate precursors are dissolved in water under continuous stirring at 50 °C. Citric acid is added to the solution in an amount corresponding to 2.5 times the number of moles of metal ions. Upon complete dissolution of citric acid, ethylene glycol is added to the solution. The molar ratio of ethylene glycol and citric acid is 1.5:1. The solution is then heated to 80 °C and stirred for 140 min. Water in the solution is subsequently evaporated until a sticky gel forms. The gel is dried overnight in a convection oven at 110 °C. The sample is then heated in a tube furnace with continuous air flow at 450 °C for 4 h and then heated to 950 °C for 8 h. For the core−shell Fe_2O_3@LSF catalyst, Fe_2O_3 nanoparticles (Sigma-Aldrich 544884, <50 nm) are weighed out corresponding to a 1:1 molar ratio of LSF to Fe_2O_3. The nanoparticles are dispersed in methanol by an ultrasonic bath. The dispersion is allowed to settle overnight, and excess methanol is drawn off the surface. The iron methanol mixture is then dispersed into water and added to the nitrate salt solution for sol−gel preparation. For the composite Fe_2O_3:LSF, excess iron nitrate, corresponding to 1:1 molar ratio of Fe_2O_3 to LSF, is added to the sol−gel preparation.

Reaction Testing. Reactivity studies are conducted in a SETARAM SETSYS Evolution Thermal Gravimetric Analyzer (TGA). Redox experiments are performed at 900 °C. The reduction and oxidation steps are performed in 10% methane balance helium and 10% oxygen balance helium, respectively. The total gas flow rate is maintained at 300 sccm/min. The oxidation and reduction steps are performed for 15 min on 50 mg of sample for 10 cycles. Samples are purged for 5 min with helium between the redox steps. For 50 cycle runs, 33 mg of each of the catalyst from the 10-cycle study are cycled for an additional 40 times. For optimization studies, the redox cycle times are varied to probe for a region with high selectivity and yield with and without reactant humidification. The products for the reduction and oxidation steps are monitored using a quadruple mass spectrometer (QMS, MKS Cirrus II).

The products are calculated by integrating the signals for the characteristic peaks of each species. The amount of CO and CO_2 produced during methane oxidation is calculated directly from the CO and CO_2 signals. Coke formation is calculated from the CO and CO_2 produced during regeneration of the catalyst in oxygen. Hydrogen attributed to coke/methane decomposition is calculated from mass balance for CO_x produced during regeneration. The balance of hydrogen produced during methane oxidation is assigned as the partial oxidation product. H_2O is calculated from a hydrogen mass balance. Selectivities are calculated using the total methane consumption determined from CO_x production in the reforming step. Hydrogen selectivity excludes hydrogen attributed to coke formation (The detailed calculation method is provided in the Supporting Information.).

For measurements such as temperature-programmed desorption and pulse reaction, a U-tube reactor is used to reduce rector dead volume and to minimize back mixing. U-tube reactor tests are performed with 200 mg of sample in a 1/4" O.D. quartz U-tube and heated by a tube furnace. A mass flow controller (MFC) valve manifold is used to pretreat the sample in the desired atmosphere. The products from the reactor are measured with the QMS. Oxygen TPD is performed by

dx.doi.org/10.1021/cs5008415 | ACS Catal. 2014, 4, 3560−3569

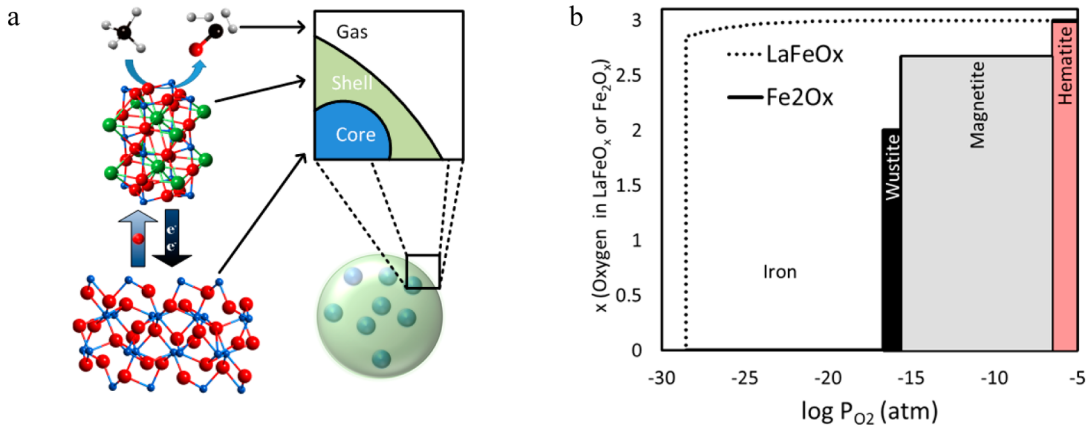

Figure 2. (a) Schematic of the core−shell redox catalyst; (b) oxygen vacancy concentrations and phase change of $LaFeO_x$ and iron oxides based on thermodynamic predictions.[41]

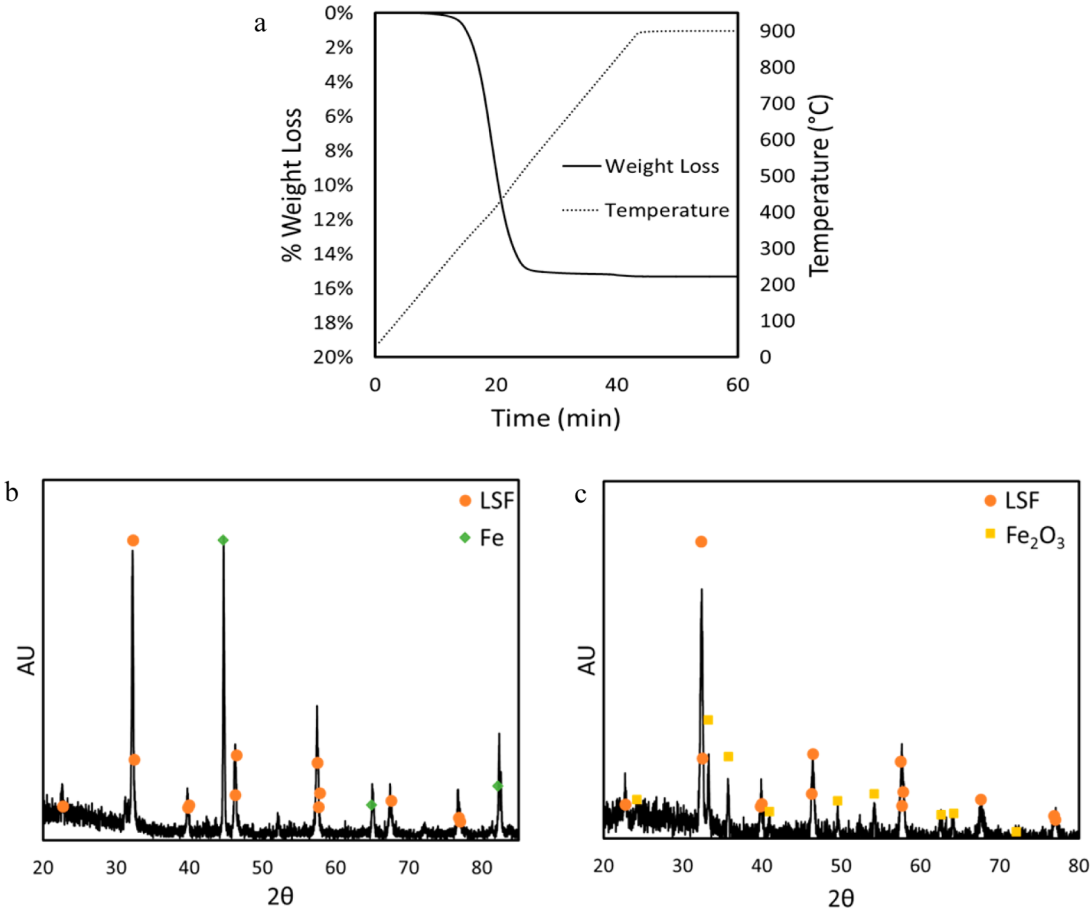

Figure 3. Core−shell TPR weight loss in H_2 (a) XRD of H_2 reduced core−shell sample (b) and XRD of 50th cycle regenerated catalyst with methane and oxygen (c). Reference patterns are taken from PDF's 00-035-1480 (ICDD, 1984), 01-076-4579 (ICDD, 2010), and 04-016-4758 (ICDD, 2011).

pretreating the sample in 20% O_2 balance helium or argon at 900 °C and cooling to 100 °C, before purging the sample in 25 sccm of argon. The reactor is then ramped at a rate of 5 °C/min to 950 °C with the effluent gas monitored by the mass spectrometer. For pulse experiments, a 1.4 mL titration loop is attached via a 6 port valve (Valco ED6UWE) upstream of the reactor, allowing for the introduction of reactant gas pulses into the system. Argon is used as sweep gas and helium as dilution gas.

Catalyst Characterization. X-ray photoelectron spectroscopy (XPS) is used to probe the near-surface composition of the fresh, 10-cycle, and 50-cycle catalysts. The system is comprised of a Thermo-Fisher Alpha 110 hemispherical energy analyzer, a Thermo-Fisher XR3, 300 W duel anode X-ray source, and a chamber with a base pressure of 1×10^{-9} Torr. A Mg anode is used. Survey spectra are taken with pass energy of 100 eV, and narrow scan spectra are taken with pass energy of 20 eV.

dx.doi.org/10.1021/cs5008415 | ACS Catal. 2014, 4, 3560−3569

Powder X-ray diffraction (XRD) is carried out to analyze the crystal phase composition before and after cycling using a Rigaku SmartLab X-ray diffractometer. A continuous scan with a 0.02° resolution is used to collect the patterns. The patterns are processed in Hi-Score Plus.

The BET surface areas are characterized using a Micromeritrics Gemini VII 2390a via a 7 point physisorption measurement at 77.3 K with nitrogen as adsorbate. Prior to testing, the samples are outgassed for 30 min at 200 °C.

RESULTS AND DISCUSSION

Design Rationale for Core−Shell Redox Catalysts and Structural Stability. While LSF can be effective for methane partial oxidation, it has limited oxygen carrying capacity (<10% wt.). In addition, high lanthanum loadings can increase the cost of the redox catalyst. The proposed core−shell concept, as illustrated in Figure 2a, has the potential to take the advantage of the high oxygen carrying capacity of low cost Fe_2O_3 and the high selectivity of LSF provided that lattice oxygen from Fe_2O_3 can be transported to and from the LSF shell in a facile manner. As indicated in Figure 2b, such a core−shell arrangement is indeed feasible from a thermodynamic standpoint since lattice oxygen in lanthanum ferrite type of perovskites is significantly more stable compared to that in iron oxides. For instance, thermodynamic calculations (*HSC Chemistry 6.0,* Chemical Software Ltd.) at 900 °C indicate that bulk hematite is reduced to magnetite, wustite, and metallic iron at oxygen partial pressure (P_{O2}) of $10^{-6.5}$, $10^{-15.6}$, and $10^{-16.7}$ atm, respectively. Lanthanum ferrite (LF), the parent perovskite of LSF, is calculated to maintain its orthorhombic structure well below 10^{-20} atm. Based on experimental data reported by Mizusaki et al.,[41] the amount of lattice oxygen release from $La_{0.75}Sr_{0.25}FeO_{3-\delta}$ is approximately 1 wt % when external P_{O2} is decreased from 0.21 atm (air) to $10^{-16.7}$ atm (wustite reduction). In comparison, iron oxide will lose approximately all of its lattice oxygen, amounting to 30 wt % under the same external P_{O2} swing. Therefore, integrating iron oxide and LSF in a core−shell form represents a thermodynamically favorable arrangement for cyclic redox operations with high oxygen carrying capacity and reduced La loading.

TGA of Fe_2O_3@LSF catalyst reduced in 10% hydrogen verifies the predicted relative stability of the core (iron oxide) and shell (LSF) materials. As can be seen from Figure 3a, the lattice oxygen loss amounts to 15.3 wt % when exposed to H_2. This corresponds to 100% reduction of the Fe_2O_3 core and reduction from $La_{0.8}Sr_{0.2}FeO_{2.85}$ to $La_{0.8}Sr_{0.2}FeO_{2.1}$. Postreduction XRD analysis confirms that LSF maintains its original perovskite structure, whereas the Fe_2O_3 core is fully reduced to metallic iron. This further confirms the ability of the core−shell sample to preferentially donate its lattice oxygen from the iron oxide core, since lattice oxygen associated with iron oxides is less stable than those in LSF. It is noted that LSF perovskite should decompose under a pure hydrogen environment from a thermodynamic standpoint. This is not observed during a 15 min reduction at 900 °C (Figure 3b). However, reduction of LSF in hydrogen for significantly longer periods does lead to decomposition (Figure S1(d)). Regeneration of the reduced core−shell redox catalyst with a 1:1 molar ratio of CO and CO_2 gives LSF and wustite phases. Magnetite and hematite phases are formed when CO_2 and air are used as the oxidation gas, respectively (see Figure S1).

In contrast to hydrogen, the LSF phase does partially decompose over periods longer than 7 min when reduced in methane. The XRD pattern of the methane reduced sample indicates that LSF separates into metallic iron, La_2O_3, and $(La_xSr_{1-x})_2FeO_4$ phases (Figure S1). Oxygen mass balances from MS measurements and TGA mass loss are also consistent with the decomposition of the LSF phase. The difference in decomposition kinetics between hydrogen and methane could be attributed to inhibition by the water formed which is strongly adsorbed on perovskite surface.

In methane, the core−shell redox catalyst exhibits 19 wt % oxygen donation, whereas pure LSF donates nearly 11 wt.% lattice oxygen. The LSF decomposition does not affect the core−shell structure of redox catalyst, as the LSF phase reassembles during regeneration over 50 cycles (Figure 3c).

Besides the ability to withdraw and redeposit lattice oxygen from and to iron oxides during cyclic redox reactions, the stability of the core−shell arrangement is important to the proposed concept. Our previous TEM study confirms the core−shell structure of sol−gel prepared Fe_2O_3@LSF.[25] XPS provides further information with respect to the surface properties and stabilities of the redox catalyst. The surface fractions of metal atoms for as-prepared and cycled samples are summarized in Table 1. For the core−shell samples, the XPS spectra indicate that the LSF phase at the catalyst surface is relatively stable over 50 redox cycles. They also indicate a reasonable LSF coating of the iron nanoparticles. The surface coverage of A-site cations (Sr and La) exceeds that of the B-site cation (Fe) for the LSF and core−shell samples throughout 50 redox cycles. This A-site enrichment is consistent with literature observations for strontium doped perovskites.[42] The composite Fe_2O_3-LSF sample exhibits higher surface Fe coverage than the core−shell. When calculated based upon the stoichiometry of LSF, only the composite exhibits less than 100% coating of the iron oxide cores. It is also noted that both LSF and core−shell samples show enrichment of strontium on the surface relative to the stoichiometry of LSF. Compared with pure LSF, the core−shell sample exhibits higher fraction of surface iron. This indicates either incomplete coating of the iron nanoparticles or a different surface stoichiometry from the pure LSF sample. Using the surface composition of pure LSF as a conservative reference, the surface LSF coverages for core−shell and composite samples are calculated and summarized in Table 2. It is notable that, despite an initial decrease in surface coverage, the LSF coating of the composite sample appears to improve over the course of 50 cycles. This may be a consequence of A-site enrichment to the perovskite surface. This enrichment of LSF to the surface indicates that the core−shell is a preferred stable structure for the LSF-iron oxide system. Additionally, this effect indicates that it may be possible to treat a composite

Table 1. Surface Atomic Fractions of Metal Cations Determined by XPS

catalyst	La	Sr	Fe
LSF as-prepared	0.37	0.33	0.30
LSF 10 cycle	0.26	0.44	0.30
LSF 50 cycle	0.28	0.40	0.32
composite as-prepared	0.35	0.21	0.45
composite 10 cycle	0.21	0.15	0.65
composite 50 cycle	0.22	0.29	0.49
core−shell as-prepared	0.33	0.26	0.41
core−shell 10 cycle	0.23	0.33	0.45
core−shell 50 cycle	0.23	0.33	0.44

dx.doi.org/10.1021/cs5008415 | ACS Catal. 2014, 4, 3560−3569

Table 2. Surface LSF Coverage Estimated Based on XPS Surface Fe^{x+} Fraction

	core−shell	composite
fresh	84%	79%
10 cycle	79%	50%
50 cycle	80%	73%

sample with redox cycles to achieve a core−shell structure while allowing for simpler synthesis techniques.

The Fe 3d XPS peaks of the core−shell and composite surface show significant broadening toward lower binding energies compared to LSF (Figure 4). This is consistent with

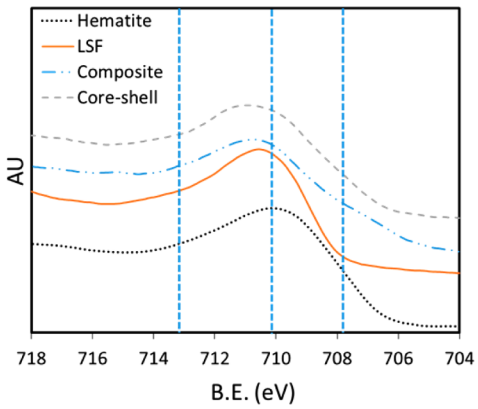

Figure 4. Fe $2p_{3/2}$ XPS spectra of the redox catalysts after 10 cycles and regenerated in oxygen; as-received hematite (NOAH SA 7.7 m^2/g) is used as the reference material (arbitrary dashed lines added for visualization).

Fe^{2+} surface species that may correspond to exposed iron oxide or oxygen deficient perovskite structures. Consistent with the presence of LSF, an Fe^{4+} like shoulder (ΔB.E. = +1.0 eV vs Fe^{3+}) is present for the core−shell sample (Figure 4). The Sr 3d and La 3d peaks of LSF (Figure 5) are consistent with similar perovskites reported in the literature,[43] with the Sr 3d showing overlapping peaks of lattice Sr and a surface carbonate. The composite and core−shell samples give rise to lower binding energy shoulders for Sr 3d and La 3d peaks. This is consistent with the formation of oxygen deficient mixed oxides. Thus, some of the surface iron seen in the core−shell and composite samples may be attributable to oxygen deficient, mixed Sr/La−Fe oxides rather than exposed iron oxide.

Redox Performance and Stability. The primary function of the proposed redox catalyst is to partially oxidize methane into CO and H_2. Table 3 summarizes the redox performance of the core−shell and composite redox catalysts in comparison with LSF. At cycle 10, the LSF catalyst exhibits the highest syngas selectivity (91% H_2, 97% CO) and forms the least coke after full reduction (3.2 mmol/g). Despite having the lowest oxygen carrying capacity, its high selectivity gives a high hydrogen yield (11.6 mmol/g). In contrast, the composite catalyst gives a lower hydrogen yield 8.6 mmol/g despite its higher oxygen carrying capacity. This is attributable to its lower selectivity, as deep oxidation of methane consumes 4 times the oxygen of partial oxidation to syngas. The 10th cycle core−shell redox catalysts give rise to syngas yields (11.5 mmol/g H_2, 6.8 mmol/g CO) comparable to pure LSF, and the hydrogen selectively (72%) is improved compared to the composite (60%). For the first ten cycles, the composite and core−shell catalysts are more prone to coke formation than pure LSF (>4 mmol/g vs 3.2 mmol/g). In the TGA of all samples, the sample weight stabilizes after 10 min, indicating a cessation of significant coke formation. The ratios of H_2 to CO production rates indicate that coke formation is only significant at the end of the reduction stage when CO production decreases. All of the catalysts exhibit good reaction stability in terms of redox reaction rates over 50 cycles. The performance of the core−shell and composite improves over the 50 cycles, whereas syngas yield from the LSF sample decreases gradually. For instance, hydrogen selectivity for the core−shell and composite samples increased to 80% and 67%, respectively. In comparison, hydrogen selectivity of pure LSF decreases from 91% to 81%. Although the core−shell has a similar yield per weight of catalyst for with lower selectivities than LSF, the economics of this system are partially driven by loading of relatively expensive lanthanum. As shown in Figure 6, the core−shell redox catalyst is capable of delivering 100% higher syngas yield over LSF when normalized with La loading in the sample.

Mechanistic Insights. Although the core−shell redox catalyst exhibits satisfactory syngas yield, mechanistic understanding of the selective (syngas production) and nonselective (combustion) oxidation of methane by the core−shell catalyst

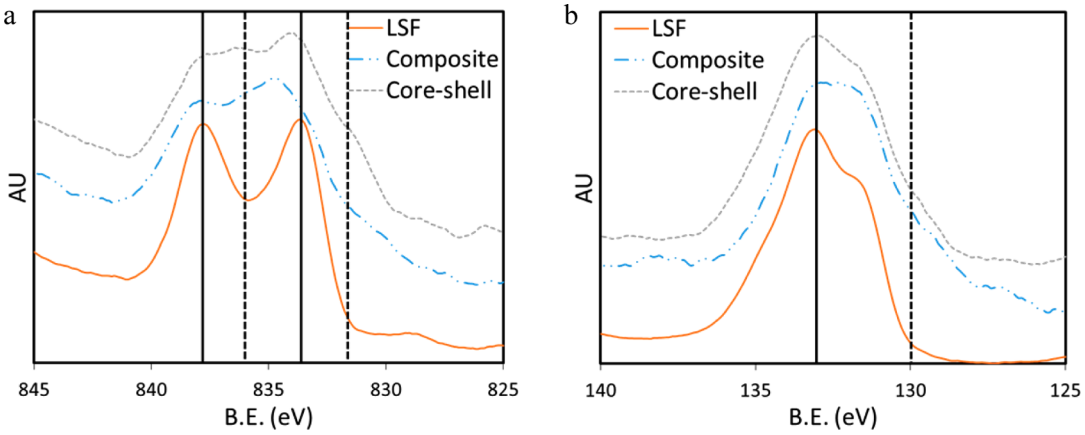

Figure 5. La $3d_{5/2}$ (a) and Sr $3d_{5/2}$ (b) XPS spectra of the redox catalysts after 10 cycles and regenerated in oxygen (solid lines represent characteristic peaks of LSF, dashed lines correspond to secondary, less electrophilic, surface species identified in composite and core−shell materials).

dx.doi.org/10.1021/cs5008415 | ACS Catal. 2014, 4, 3560−3569

Table 3. Syngas Yields and Selectivity over 50 Redox Cycles for LSF, Composite, and Core−Shell Redox Catalysts[a]

	LSF		composite		core−shell	
	10th cycle	50th cycle	10th cycle	50th cycle	10th cycle	50th cycle
H_2 (POx)	11.6 (91%)	9.8 (81%)	8.6 (60%)	10.2 (67%)	11.5 (72%)	12.4 (80%)
H_2 (coke)	6.3	4.4	8.3	8.3	8.8	6
H_2O	0.87	2.3	5.5	5.0	3.6	2.8
CO	6.0 (97%)	5.9 (99%)	5.7 (79%)	6.5 (86%)	6.1 (80%)	6.1 (87%)
CO_2	0.22	0.08	1.5	1.1	1.5	1.0
coke	3.2	2.2	4.2	4.2	4.4	3.0
methane consumption	9.4	8.2	11.4	11.8	12.0	10.3

[a]Units for yields are in mmol/g, selectivity values are given in brackets. Selectivity is calculated by mass balance of CO_x products during reforming. H_2 (POx) selectivity excludes hydrogen attributed to coke formation (H_2 (coke)).

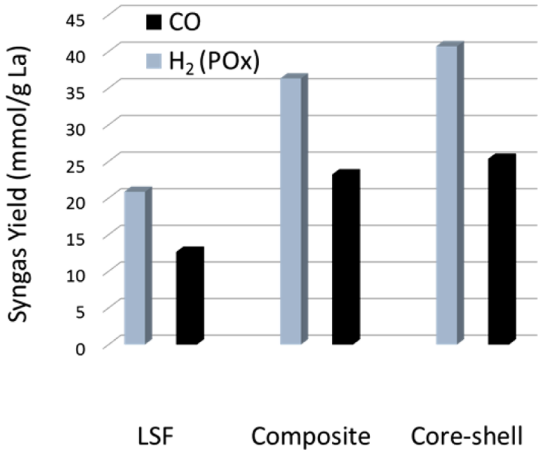

Figure 6. Normalized syngas yield from the redox catalysts based on cycle 50 results.

is highly desired in order to further increase catalyst performance. Figure 7 shows a time-dependent product profile from a typical reduction cycle of the core−shell redox catalyst. As can be seen, the reduction of the core−shell catalyst can be divided into four distinct regions based on syngas yield and selectivity: (i) an initial region dominated by deep oxidation; (ii) a transition region of competing deep and selective oxidation; (iii) a selective oxidation region of increasing activity; and (iv) a coking region dominated by methane decomposition. In comparison, pure LSF only displays some activity for deep oxidation at the beginning of the reaction (Figure S2). The increase in activity, or "autoactivation", observed in region iii for the core−shell catalyst, also appears for pure LSF, albeit at an earlier stage.

Demarcation of the Reaction Regions and Role of Oxygen Conduction. Figure 8 compares weight loss of the core−shell catalyst calculated from experimental data and the corresponding phases from theoretical prediction (based on thermodynamic data from HSC and ref 32). As can be seen, regions i-ii and iii-iv transitions appear to correlate with the average oxidation state of iron in the core. The demarcation of

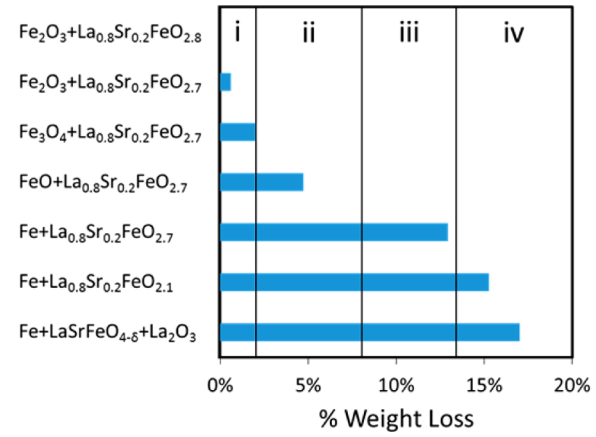

Figure 8. Core−shell redox catalyst weight loss for the four regions and corresponding phases calculated based on thermodynamic prediction of average oxidation states (see Figure 2b).

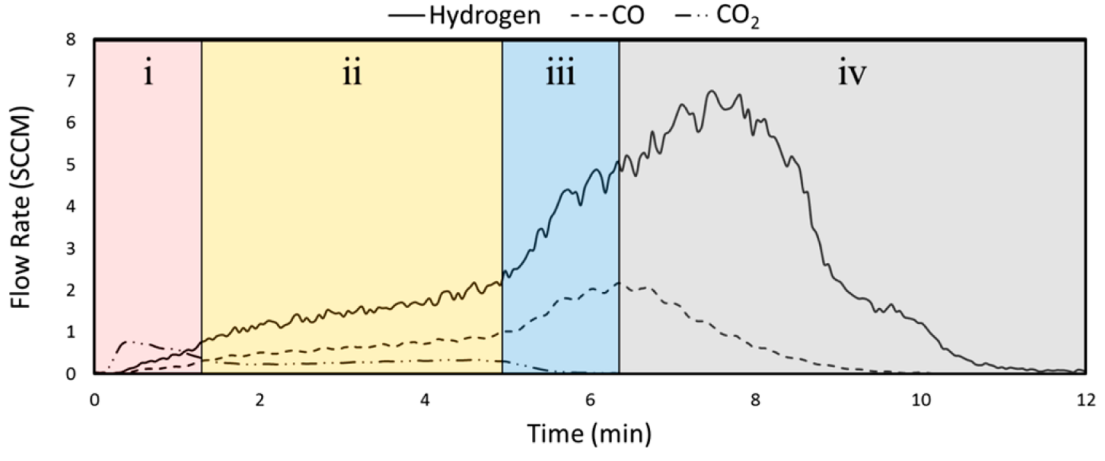

Figure 7. Temporal yields of gaseous products during the reduction of Fe_2O_3@LSF with methane.

dx.doi.org/10.1021/cs5008415 | ACS Catal. 2014, 4, 3560−3569

regions i and ii aligns with the depletion of hematite to Fe_3O_4. The highly selective region iii corresponds to a coexistence of metallic iron and wustite phases. The transition from region iii to iv roughly corresponds to the predicted depletion of oxygen from the iron phase. Thus, decomposition of LSF is likely to occur in region iv. The corresponding precipitation of metallic iron that occurs during LSF decomposition would catalyze methane decomposition and coke formation. The higher propensity of the composite sample to coke vs pure LSF indicates that higher availability of metallic iron may lead to increased coke formation.

These demarcations, based on average oxidation state of iron, represent the true oxidation state of iron throughout the catalyst particle only if oxygen conduction is significantly faster than surface reactions, as proposed by Mihai et al. for $LaFeO_{3-\delta}$.[35] In the cases when the overall reduction rate is limited by oxygen conduction, a significant concentration gradient of O^{2-} is expected in order to drive the O^{2-} flux toward the catalyst surface for methane conversion. This corresponds to higher oxidation state of Fe in the bulk compared to the surface. Conversely, a higher iron oxidation state at the surface compared to the bulk would be anticipated during regeneration if O^{2-} conduction is rate-limiting. Since oxygen bonded iron (Fe^{x+}) are known to be selective toward deep oxidation of methane,[17] comparing syngas selectivity of a partially regenerated catalyst with that under continuous reduction can reveal the importance of O^{2-} conduction. If O^{2-} conduction is fast, identical selectivity should be anticipated for samples with identical average oxidation state irrespective to how they are prepared. Under an O^{2-} transport limited scenario; however, one would expect lower syngas selectivity for the regenerated sample since it corresponds to higher surface oxidation state of iron. The importance of O^{2-} conduction is verified by using CO_2 to reoxidize a fully reduced core−shell catalyst sample. XRD confirms the presence of Fe_3O_4 as the primary ferrite phase. From its average oxidation state in Figure 8, the sample should exhibit syngas selectivity comparable to that in region ii. Experimental results, however, indicate that the regenerated sample exhibits significantly lower syngas selectivity (20%) compared to that of a continuously reduced sample at an identical oxidation state (>80%) (Figure S2). These results indicate O^{2-} transport limitation and O^{2-} gradient in the catalyst.

Pulse experiments further confirm the O^{2-} transport limitation in region ii (Figure 9). When a partially reduced core−shell catalyst is exposed to a rapid succession of methane pulses (20 s apart), CO selectivity improves from 70% to 76% over 10 pulses. When the system is allowed to relax during a 2 min of inert purge, a lower CO selectivity of 73% is observed. This indicates that a high relaxation time allows for O^{2-} conduction from the bulk to the surface, leading to higher surface oxygen coverage and less selective Fe^{x+} species. Additionally, calculation of oxygen consumption rate (Figure S2d) shows only a minor discontinuity in oxygen flux to the catalyst surface. This also suggests significant O^{2-} gradient in the sample, since one would anticipate step changes in O^{2-} flux provided that phase change in the catalyst core occur in a uniform, stepwise manner. The region transitions, thus, appear to be dependent upon oxygen availably at the catalyst surface, which is determined by both the diffusive flux of O^{2-} and its availability in the bulk (as determined by average oxidation state).

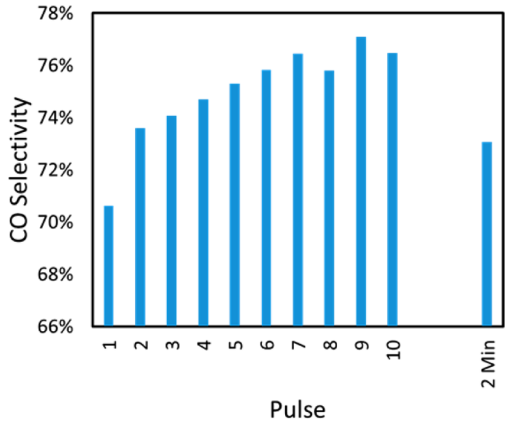

Figure 9. CO selectivity of sequential 0.85 mL methane pulses over partially reduced core−shell redox catalyst.

The apparent transport dependence of the reaction regions differs from the previously reported perovskite catalysts. For instance, Mihai et al. proposed, for $LaFeO_{3-\delta}$ based oxygen carriers, that the surface structure controls surface oxygen vacancies, which in turn determines product selectivity.[35] This mechanism assumes that bulk lattice oxygen transfer is significantly faster than the surface reaction. However, such an assumption is not valid for the core−shell redox catalyst based on the aforementioned data. O^{2-} transport limitation in the core−shell redox catalyst is understandable since additional mass transfer resistances can exist within the iron oxide core and across the iron oxide-perovskite phase boundaries. If the 50 nm diameter particle is approximated as 25 nm slabs, ionic oxygen transport is estimated to have diffusion time scales (L^2/D) within the iron oxide cores of 5 s or more depending on the oxidation state.[44] Even with the presence of transport limitations, the average oxygen donation rate of the core−shell catalyst (20 mg/g/min) is comparable to that of the pure LSF catalyst (22 mg/g/min). Considering the significantly higher active-O^{2-} storage capacity in the core−shell catalyst, the core−shell design can potentially be highly effective for oxygen transfer and storage.

Surface and Bulk Species for Deep and Partial Oxidations. Among the four reaction regions, regions i and iii are of particular interest since either eliminating region i or confining the catalyst to region iii will improve catalyst selectivity. Deep oxidation seen in region i is typically attributed to surface oxygen.[29,34,35] The mechanism for deep oxidation has been explained as either contiguous surface oxygen[35] or chemisorbed oxygen species.[45] Indeed, chemisorbed oxygen peaks can be observed in the oxygen TPD of the core−shell catalyst (Figure S5). However, the relatively small surface area of cycled core−shell redox catalyst (4.1 m^2/g) does not possess adequate chemisorbed oxygen or contiguous oxygen to be solely responsible for amount of deep oxidation products. For example, the atomic oxygen density of an oxygen rich LSF crystallographic plane (~0.076 nm^2/atom in the (002) plane) would give less than 0.09 mmol/g of surface oxygen atoms. Oxygen eluted from TPD corresponds to ~8 μmol/g of catalyst (Figure S5). In comparison, 2 mmol/g oxygen ions is required to form the amount of CO_2 alone.

Exposed surface iron from incomplete coating could contribute to deep oxidation, as hematite is active for deep oxidation of methane.[28] However, the rate of reaction in the core−shell and composite is exceptional. XPS and BET

dx.doi.org/10.1021/cs5008415 | ACS Catal. 2014, 4, 3560−3569

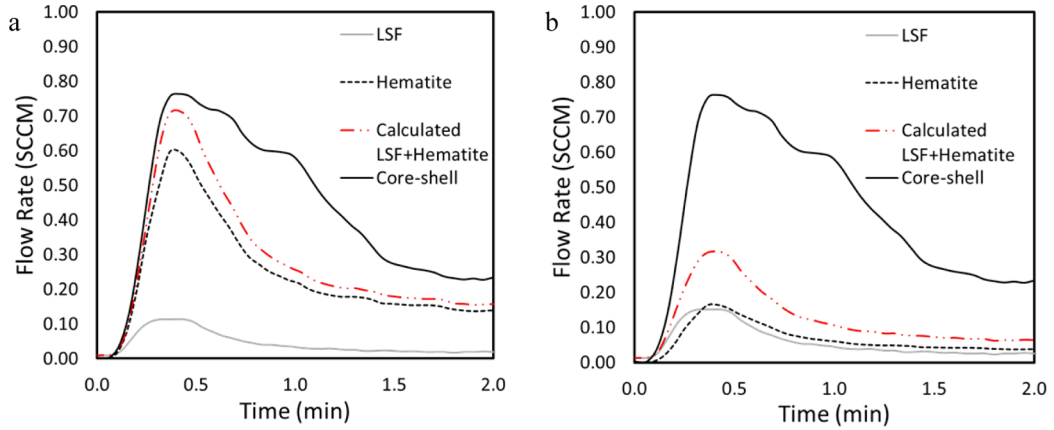

Figure 10. Region i CO_2 production for core−shell component vs LSF and hematite components by (a) weight and (b) surface area.

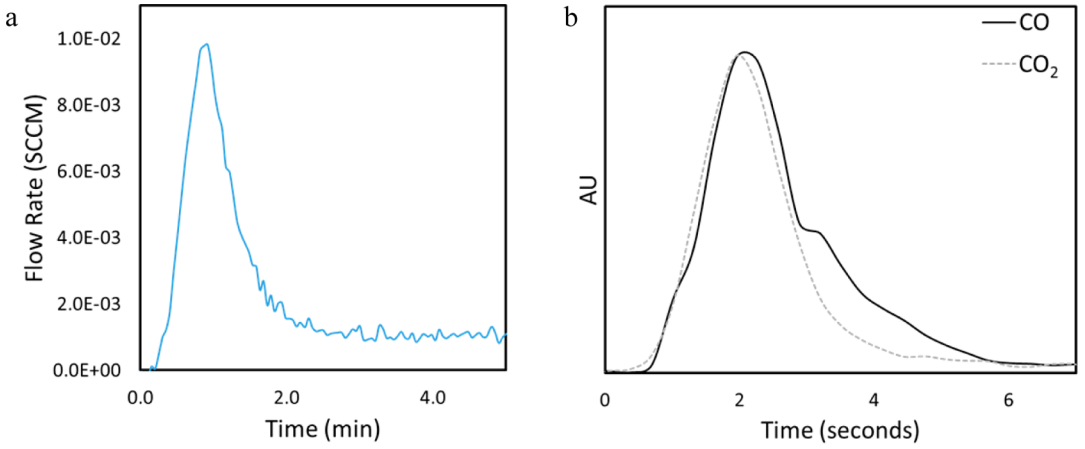

Figure 11. CO desorption peak of partially reduced LSF at 900 C (a) and CO and CO_2 elution from 0.85 mL methane pulse over a core−shell sample partially reduced to region ii (b).

measurements do not indicate adequate surface hematite phase to be directly responsible for the deep oxidation. Compared to the activity of a commercial hematite powder (NOAH SA 7.7 m^2/g), deep oxidation in the core−shell sample in region i is exceptional on the basis of both hematite weight fraction (40%) and exposed surface area (~20% from XPS) (Figure 10).

The high rate of deep oxidation in regions i and ii also proceeds well past where adsorbed oxygen should be available. LSF, thus, appears to be conveying oxygen that is active for deep oxidation from iron oxide nanoparticles to the catalyst surface. While chemisorbed oxygen could still contribute to ~1% of the deep oxidation products, the primary source of oxygen for deep oxidation is better attributed lattice oxygen that can evolve into surface oxygen species such as O^- (hereafter referred to as "loose" lattice oxygen):

$$O^{2-}_{Bulk} \leftrightarrow O^{2-}_{Surface} \leftrightarrow O^{-}_{Surface} + e^-$$

In pure LSF, the system would move quickly toward depletion of such oxygen anions. In comparison, iron oxide in the core−shell catalyst can serve as a larger reservoir of such "loose" lattice oxygen. This is consistent with the high chemical potential of O^{2-} in iron oxides (Figure 2b) and facile transport of O^{2-} though the LSF support.

Region iii is characterized by high syngas selectivity (>95%) and increasing activity with increasing extent of reduction. In the literature, it has been reported that methane partial oxidation over perovskite is surface rate limited.[35] The core−shell catalyst behavior suggests a more complex mechanism. Despite losing significant surface area over the course of 50 cycles (8.7 to 4.1 for the core−shell), the core−shell catalysts syngas productivity does not change significantly, and the autoactivation does not onset until well after significant amounts of oxygen have been extracted from the sample. This suggests that surface autoactivation occurs when oxygen transport becomes rate limiting, promoting formation of a highly active surface. The lack of a strong effect of surface area on the apparent reaction kinetics indicates that surface reaction and intraparticle diffusion are not likely to be the rate limiting steps for the redox reactions (see also Figures S3 and S4).

The nature of the active surface in region iii is suggested by CO chemisorption on a H_2 reduced core−shell catalyst. While the fully oxidized catalyst does not adsorb a significant amount of CO, a CO desorption peak is observed for a partially reduced sample (H_2, Figure 11). Additionally, during pulses of methane through a core−shell catalyst reduced to region ii, there is a significant shoulder of CO, indicating the surface interacts strongly with CO or its precursor. This points to the formation of a reduced iron phase on the catalyst surface. While the surface metallic iron is likely to be responsible for the partial oxidation reaction,[35] its formation is controlled by a combination of O^{2-} diffusivity, gas phase oxygen partial pressure (P_{O2}), and bulk O^{2-} availability. Therefore, O^{2-} conduction and availability play a crucial role in terms of syngas selectivity.

dx.doi.org/10.1021/cs5008415 | ACS Catal. 2014, 4, 3560−3569

Catalyst Optimization. The aforementioned mechanistic findings indicate that higher syngas selectivity and lower coke formation can potentially be achieved by controlling the oxidation state of iron through partial redox cycles. Considering the effect of O^{2-} transport limitations and surface O^{2-} enrichment during the regeneration step, region i can be avoided by regenerating the iron oxide core to FeO, whereas region iv can be avoided by incomplete reduction of the catalyst. To validate the feasibility and potential advantages of partial redox cycles, a low concentration of steam (2% of flow) is added to the reaction gas to regulate the redox reactions. As shown in Figure 12, both region i and region iv are completely

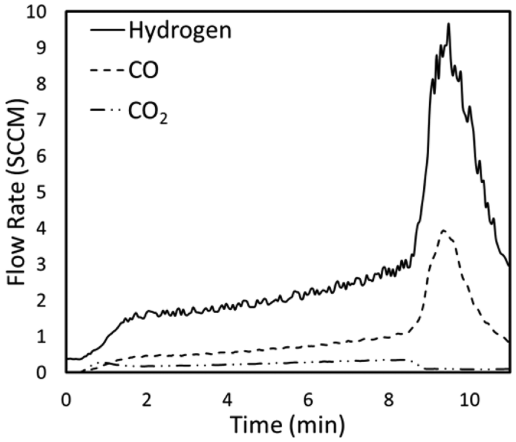

Figure 12. Reduction of partially regenerated core−shell catalyst in 20% methane 2% H_2O.

avoided under partial redox cycles. H_2 and CO productivity of 29.8 mmol/g and 9.4 mmol/g are achieved without coke formation. This corresponds to more than 100% increase in syngas productivity. Excluding hydrogen from steam (see Table S1), the overall syngas selectivity is estimated to be greater than 90%. Although complete avoidance of regions i and iv may not be easily achievable in commercial reactors, the findings in the current study can help determine suitable reactor design and operating conditions for improved catalyst performance.

CONCLUSIONS

This article investigates the feasibility and underlying mechanism for methane partial oxidation over an Fe_2O_3@LSF core−shell redox catalyst. The results indicate that the higher stability of lattice oxygen in LSF compared to that in iron oxides allows effective O^{2-} removal and redeposition from and to the iron oxide core. Compared to an Fe_2O_3:LSF composite redox catalyst, the core−shell catalyst is more active and selective. On a lanthanum loading basis, the core−shell redox catalyst delivers a syngas yield nearly 100% higher than that of LSF perovskite alone. The excellent performance of the LSF@Fe_2O_3 redox catalyst results from its stability and mixed ionic-electronic conductivity, which allows facile lattice oxygen transport between iron oxide particles and the shell surface. XRD and XPS studies indicate that the core−shell structure remains intact over 50 redox cycles.

The reaction between methane and the core−shell redox catalyst can be divided into four distinct regions: i. deep oxidation, ii. competing selective and deep oxidation, iii. selective oxidation with autoactivation, and iv. methane decomposition/coke formation. Further investigation of these reaction regions reveals an O^{2-}-conduction limited, highly dynamic reaction scheme. For instance, the primary source of oxygen for deep oxidation in region i is attributed to "loose" lattice oxygen from the iron oxide cores, which is transported and evolved into surface oxygen species. In region ii, both selective and nonselective oxygen species compete for methane oxidation, with the product ratio determined by O^{2-} flux and overall oxygen availability. Resulting from continued oxygen consumption, region iii is characterized by a further decrease in surface oxygen concentration and an increase in metallic iron species on the surface. Coke formation in region iv corresponds to depletion of O^{2-} in the iron oxide core and methane decomposition over metallic iron precipitated from LSF lattice. Overall, the activity and selectivity of the core−shell redox catalyst is directly affected by the type and concentration of surface oxygen species. The latter, however, is controlled by a combination of O^{2-} diffusivity and bulk O^{2-} availability. Based on such mechanistic insights, it is shown that limiting the extent of reduction and oxidation during the redox cycles can eliminate coke formation while significantly increasing syngas selectivity and yield from methane conversion.

ASSOCIATED CONTENT

Supporting Information

Further XRD of the core−shell catalyst, time profiles of methane reduction products over select catalysts, and oxygen TPD of the core−shell. This material is available free of charge via the Internet at http://pubs.acs.org.

AUTHOR INFORMATION

Corresponding Author

*E-mail: fli5@ncsu.edu.

Notes

The authors declare no competing financial interest.

ACKNOWLEDGMENTS

This work was supported by the U.S. National Science Foundation (award no. CBET-1254351). We acknowledge the use of the Analytical Instrumentation Facility (AIF) at North Carolina State University, which is supported by the State of North Carolina and the National Science Foundation. We acknowledge Prof. Jeffery T. Glass at Duke University for sharing his XPS facilities. We also acknowledge Feng He, Elizabeth Shively, and Kit Yeung, who helped to set up the experimental apparatus and run some of the experiments.

REFERENCES

(1) Bao, B.; El-Halwagi, M. M.; Elbashir, N. O. *Fuel Process. Technol.* **2010**, *91*, 703−713.
(2) Krishna, R.; Ellenberger, J.; Sie, S. T. *Chem. Eng. Sci.* **1996**, *51*, 2041−2050.
(3) Elia, J. A.; Baliban, R. C.; Xiao, X.; Floudas, C. A. *Comput. Chem. Eng.* **2011**, *35*, 1399−1430.
(4) Rahimpour, M. R.; Mirvakili, A.; Paymooni, K. *Energy* **2011**, *36*, 1223−1235.
(5) Ab Rahim, M. H.; Forde, M. M.; Jenkins, R. L.; Hammond, C.; He, Q.; Dimitratos, N.; Lopez-Sanchez, J. A.; Carley, A. F.; Taylor, S. H.; Willock, D. J.; Murphy, D. M.; Kiely, C. J.; Hutchings, G. J. *Angew. Chem.* **2013**, *125*, 1318−1322.
(6) Hammond, C.; Forde, M. M.; Ab Rahim, M. H.; Thetford, A.; He, Q.; Jenkins, R. L.; Dimitratos, N.; Lopez-Sanchez, J. A.; Dummer, N. F.; Murphy, D. M.; Carley, A. F.; Taylor, S. H.; Willock, D. J.; Stangland, E. E.; Kang, J.; Hagen, H.; Kiely, C. J.; Hutchings, G. J. *Angew. Chem., Int. Ed.* **2012**, *51*, 5129−5133.

(7) Arndt, S.; Otremba, T.; Simon, U.; Yildiz, M.; Schubert, H.; Schomäcker, R. *Appl. Catal. Gen.* **2012**, *425*−*426*, 53−61.
(8) Elkins, T. W.; Hagelin-Weaver, H. E. *Appl. Catal.,A* **2013**, *454*, 100−114.
(9) Das, T. N.; Dey, G. R. *J. Hazard. Mater.* **2013**, *248*−*249*, 469−477.
(10) Cao, Z.; Jiang, H.; Luo, H.; Baumann, S.; Meulenberg, W. A.; Assmann, J.; Mleczko, L.; Liu, Y.; Caro, J. *Angew. Chem.* **2013**, *125*, 14039−14042.
(11) Guo, X.; Fang, G.; Li, G.; Ma, H.; Fan, H.; Yu, L.; Ma, C.; Wu, X.; Deng, D.; Wei, M.; Tan, D.; Si, R.; Zhang, S.; Li, J.; Sun, L.; Tang, Z.; Pan, X.; Bao, X. *Science* **2014**, *344*, 616−619.
(12) Rostrup-Nielsen, J. R. *Catal. Today* **2000**, *63*, 159−164.
(13) Eilers, J.; Posthuma, S. A.; Sie, S. T. *Catal. Lett.* **1990**, *7*, 253−269.
(14) Khodakov, A. Y.; Chu, W.; Fongarland, P. *Chem. Rev.* **2007**, *107*, 1692−1744.
(15) Wilhelm, D. J.; Simbeck, D. R.; Karp, A. D.; Dickenson, R. L. *Fuel Process. Technol.* **2001**, *71*, 139−148.
(16) Adanez, J.; Abad, A.; Garcia-Labiano, F.; Gayan, P.; de Diego, L. F. *Prog. Energy Combust. Sci.* **2012**, *38*, 215−282.
(17) Li, F.; Zeng, L.; Ramkumar, S.; Sridhar, D.; Iyer, M.; Fan, L.-S.; Fan, L.-S. In *Chemical Looping Systems for Fossil Energy Conversions*; John Wiley & Sons, Inc.: 2010; pp 215−300.
(18) Rydén, M.; Lyngfelt, A.; Mattisson, T. *Fuel* **2006**, *85*, 1631−1641.
(19) Thursfield, A.; Murugan, A.; Franca, R.; Metcalfe, I. S. *Energy Environ. Sci.* **2012**, *5*, 7421−7459.
(20) Bhavsar, S.; Najera, M.; Solunke, R.; Veser, G. *Catal. Today* **2014**, *228*, 96−105.
(21) De Diego, L. F.; Ortiz, M.; Adánez, J.; García-Labiano, F.; Abad, A.; Gayán, P. *Chem. Eng. J.* **2008**, *144*, 289−298.
(22) Johansson, M.; Mattisson, T.; Lyngfelt, A.; Abad, A. *Fuel* **2008**, *87*, 988−1001.
(23) Zhou, Z.; Han, L.; Bollas, G. M. *Int. J. Hydrogen Energy* **2014**, *39*, 8535−8556.
(24) Oller, A. R.; Costa, M.; Oberdörster, G. *Toxicol. Appl. Pharmacol.* **1997**, *143*, 152−166.
(25) Shafiefarhood, A.; Galinsky, N.; Huang, Y.; Chen, Y.; Li, F. *ChemCatChem* **2014**, *6*, 790−799.
(26) ten Elshof, J. E.; Lankhorst, M. H. R.; Bouwmeester, H. J. M. *J. Electrochem. Soc.* **1997**, *144*, 1060−1067.
(27) Patrakeev, M. V.; Bahteeva, J. A.; Mitberg, E. B.; Leonidov, I. A.; Kozhevnikov, V. L.; Poeppelmeier, K. R. *J. Solid State Chem.* **2003**, *172*, 219−231.
(28) Galinsky, N. L.; Huang, Y.; Shafiefarhood, A.; Li, F. *ACS Sustainable Chem. Eng.* **2013**, *1*, 364−373.
(29) Readman, J. E.; Olafsen, A.; Larring, Y.; Blom, R. *J. Mater. Chem.* **2005**, *15*, 1931.
(30) McCarty, J. G.; Wise, H. *Catal. Today* **1990**, *8*, 231−248.
(31) Slagtern, Å.; Olsbye, U. *Appl. Catal. Gen.* **1994**, *110*, 99−108.
(32) Dai, H. X.; Ng, C. F.; Au, C. T. *J. Catal.* **2000**, *189*, 52−62.
(33) Dai, X. P.; Wu, Q.; Li, R. J.; Yu, C. C.; Hao, Z. P. *J. Phys. Chem. B* **2006**, *110*, 25856−25862.
(34) Dai, X.; Yu, C.; Li, R.; Wu, Q.; Shi, K.; Hao, Z. *J. Rare Earths* **2008**, *26*, 341−346.
(35) Mihai, O.; Chen, D.; Holmen, A. *J. Catal.* **2012**, *293*, 175−185.
(36) He, F.; Li, X.; Zhao, K.; Huang, Z.; Wei, G.; Li, H. *Fuel* **2013**, *108*, 465−473.
(37) Imtiaz, Q.; Hosseini, D.; Müller, C. R. *Energy Technol.* **2013**, *1*, 633−647.
(38) Li, F.; Fan, L.-S. *Energy Environ. Sci.* **2008**, *1*, 248−267.
(39) He, F.; Trainham, J.; Parsons, G.; Newman, J. S.; Li, F. *Energy Environ. Sci.* **2014**, *7*, 2033−2042.
(40) Chen, Y.; Galinsky, N.; Wang, Z.; Li, F. *Fuel* **2014**, *134*, 521−530.
(41) Mizusaki, J.; Yoshihiro, M.; Yamauchi, S.; Fueki, K. *J. Solid State Chem.* **1985**, *58*, 257−266.
(42) Pai, M. R.; Wani, B. N.; Sreedhar, B.; Singh, S.; Gupta, N. M. *J. Mol. Catal. A: Chem.* **2005**, *246*, 128−135.
(43) Thermo Fisher Scientific. Application Note: 52110.
(44) Millot, F.; Yan, N. *J. Phys. Chem. Solids* **1997**, *58*, 63−72.
(45) Arai, H.; Yamada, T.; Eguchi, K.; Seiyama, T. *Appl. Catal.* **1986**, *26*, 265−276.